Monthly Notices
of the
ROYAL ASTRONOMICAL SOCIETY

MNRAS **463,** 820–831 (2016)
Advance Access publication 2016 August 10

doi:10.1093/mnras/stw1992

The X-ray luminosity–temperature relation of a complete sample of low-mass galaxy clusters

S. Zou,[1,2]★ B. J. Maughan,[1] P. A. Giles,[1] A. Vikhlinin,[3,4] F. Pacaud,[5] R. Burenin[4,6] and A. Hornstrup[7]

[1]*HH Wills Physics Laboratory, University of Bristol, Tyndall Avenue, Bristol BS8 1TL, UK*
[2]*Institut d'Astrophysique de Paris, Université Paris 6, CNRS-UMR7095, 98bis Boulevard Arago, F-75014 Paris, France*
[3]*Harvard-Smithsonian Center for Astrophysics, 60 Garden Street, Cambridge, MA 02140, USA*
[4]*Space Research Institute, Russian Academy of Sciences, Profsoyuznaya ul. 84/32, Moscow 117997, Russia*
[5]*Argelander-Institut fur Astronomie, University of Bonn, Auf dem Hugel 71, D-53121 Bonn, Germany*
[6]*Moscow Institute of Physics and Technology, Dolgoprudny, Institutsky per., 9, 141700, Russia*
[7]*National Space Institute, Technical University of Denmark, Juliane Maries Vej 30, DK-2100 Copenhagen 0, Denmark*

Accepted 2016 August 8. Received 2016 August 3; in original form 2015 November 23

ABSTRACT

We present *Chandra* observations of 23 galaxy groups and low-mass galaxy clusters at $0.03 < z < 0.15$ with a median temperature of ∼2keV. The sample is a statistically complete flux-limited subset of the 400 deg^2 survey. We investigated the scaling relation between X-ray luminosity (L) and temperature (T), taking selection biases fully into account. The logarithmic slope of the bolometric L–T relation was found to be 3.29 ± 0.33, consistent with values typically found for samples of more massive clusters. In combination with other recent studies of the L–T relation, we show that there is no evidence for the slope, normalization, or scatter of the L–T relation of galaxy groups being different than that of massive clusters. The exception to this is that in the special case of the most relaxed systems, the slope of the core-excised L–T relation appears to steepen from the self-similar value found for massive clusters to a steeper slope for the lower mass sample studied here. Thanks to our rigorous treatment of selection biases, these measurements provide a robust reference against which to compare predictions of models of the impact of feedback on the X-ray properties of galaxy groups.

Key words: methods: observational – methods: statistical – galaxies: clusters: general – galaxies: clusters: intracluster medium – galaxies: groups: general – X-rays: galaxies: clusters.

1 INTRODUCTION

Galaxy clusters are the largest gravitationally bound systems in the Universe, ranging in size from 2–10 Mpc, with X-ray luminosities of $\sim 10^{43}$–10^{45} erg s^{-1}. The mass content of clusters consists of ∼85 per cent dark matter, ∼12 per cent X-ray bright, low-density intracluster medium (ICM) and ∼3 per cent stars. Studying galaxy clusters is motivated by two complementary goals, investigating the formation and evolution of clusters and their galaxies, and using clusters as cosmological probes.

If the ICM is only heated by the conversion, via shocks, of its gravitational potential energy to internal energy during its infall into the cluster, then its properties will exhibit self-similar behaviour. This will lead to simple power-law correlations between the X-ray observables, such as the temperature (T) and luminosity (L) of the gas (Kaiser 1986). Importantly, any deviations of observed clusters from this self-similar behaviour points to the action of non-gravitational energy input to the ICM, such as mechanical and radiative energy from supernova-driven galaxy winds, or outflows powered by active galactic nuclei (AGN).

The correlation between X-ray luminosity and temperature (the L–T relation) has been extensively studied, due to the relative ease with which those properties can be measured (e.g. Edge & Stewart 1991; Markevitch 1998; Pratt et al. 2009; Maughan et al. 2012; Bharadwaj et al. 2015; Lovisari, Reiprich & Schellenberger 2015). A consensus has emerged that the L–T relation is steeper than the self-similar prediction, in the sense that lower mass clusters are hotter and/or less luminous than expected [although Maughan et al. (2012) found evidence that the most massive, relaxed clusters show self-similar behaviour when their core regions are ignored]. This is interpreted as evidence that non-gravitational heating has a stronger impact on the ICM in low-mass haloes, where the gravitational potential is weaker, leading to similarity breaking.

★ E-mail: sz13769@my.bristol.ac.uk

Further evidence for the presence of non-gravitational heating in groups and clusters is provided by observations of cluster cores. In core regions, the high ICM density leads to cooling times that are short relative to the cluster's lifetime. This should establish a cooling flow, wherein cooling, condensing gas in the cluster core is replaced by a slow inflow of gas from larger radii, which itself cools as it flows into the core (see Fabian 1994, for a review). The high cooling rates expected in this scenario have not been observed, with observations demonstrating that the ICM in these cool cores (CCs) is being prevented from cooling fully out of the X-ray emitting regime in large quantities (e.g. Peterson & Fabian 2006).

The favoured mechanism for balancing cooling in cluster cores is energy input from AGN, based on evidence including the large fraction of CC clusters that possess AGN which show signs of interacting with the ICM by blowing cavities, and plausibility arguments that the energy associated with these cavities (and in some cases, related shocks) is sufficient to balance cooling (see e.g. Churazov et al. 2002; McNamara & Nulsen 2007; Panagoulia et al. 2014; Randall et al. 2015).

It is thus plausible that AGN input is responsible for both breaking self-similarity in clusters, and balancing cooling in their cores. An emerging model is that two modes of AGN feedback are at work (as reviewed in Fabian 2012). Cooling appears to be balanced by ongoing mechanical energy input from the AGN, forming a feedback loop with the accretion of cooling gas on to the central galaxy. It is proposed that self-similarity was broken by a form of AGN heating that raised the entropy of the gas in clusters, reducing its density (and hence X-ray luminosity) and removing it towards or beyond the virial radius of the cluster. It is unclear if this heating occurred in the form of energy input through winds or outbursts at high redshifts, or steady continuous feedback over time. It is also possible that excess energy from the ongoing mechanical feedback, beyond that required to balance cooling, could play a role in similarity breaking over the lifetime of the cluster (Hlavacek-Larrondo et al. 2015). Studying the ICM properties of cluster populations as a function of mass and redshift can discriminate between, and refine these feedback models.

The study of the *L–T* relation in low-mass clusters and galaxy groups thus has the potential to give clues to the nature of the non-gravitational processes that break self-similarity. However, measuring the *L–T* relation in groups is more challenging than for clusters because of their lower intrinsic luminosities. Progress has been made, albeit without yet reaching the same level of consensus that is found in the higher mass regime. Earlier studies have variously found that the *L–T* relation in groups is consistent with (e.g. Mulchaey & Zabludoff 1998; Osmond & Ponman 2004) or steeper than (e.g. Helsdon & Ponman 2000) that in clusters.

Some of the variety in results may be due to the composition of the samples that have been studied. Groups and clusters undergoing mergers trace stochastic paths on the *L–T* plane as the merger progresses (Rowley, Thomas & Kay 2004). Meanwhile, the presence of CCs in systems leads to large offsets in the *L–T* plane relative to those without CCs (e.g. Markevitch 1998). These effects contribute to significant scatter in the *L–T* plane, and can lead to disparate results if non-representative samples of clusters are studied. More recently, the importance of selection biases on the determinations of cluster scaling relations has been recognized, which could have significant effects in the low-mass regime, where the scatter in observables is expected to be large. Studies that have attempted to correct for selection biases on the *L–T* relation appear to be converging to show that the slope of the *L–T* relation is consistent between clusters and groups (Mantz et al. 2010; Bharadwaj et al. 2015; Lovisari et al. 2015).

In this paper, we investigate the *L–T* relation of a complete sample of groups and low-mass clusters selected from the 400 square degree survey (400 d; Burenin et al. 2007). Our work is comparable with other recent studies of the *L–T* relation in this low-mass regime (Bharadwaj et al. 2015; Lovisari et al. 2015), but we employ what is arguably the most rigorous treatment of selection biases used in this mass range, comparable with the approach of Mantz et al. (2010) for higher mass clusters. The sample studied in Bharadwaj et al. (2015, hereafter B14) comprised 26 groups taken from several cluster surveys based on *ROSAT* all-sky survey (RASS) data, and that had available *Chandra* observations (as described in Eckmiller, Hudson & Reiprich 2011). The selected groups have a redshift range $0.01 < z < 0.05$, and temperatures in the range $0.6 \leq T \leq 3.6$ keV. The work of Lovisari et al. (2015, hereafter L14) is based on a sample selected in a similar way from RASS-based surveys, but they were able to construct a complete flux-limited sample of 23 clusters with *XMM–Newton* observations. The resulting sample had a redshift range $0.01 < z < 0.04$ and temperature range $0.85 \leq T \leq 2.80$ keV. The B14 and L14 samples have eight groups in common with each other, but neither overlap with our 400 d groups sample.

This paper is organized as follows: we describe the sample and its analysis in Section 2; we present *L–T* relation both with and without correction for selection biases in Sections 3 and 4; in Section 5, we discuss our results and compare them with other recent work; finally, the key results are summarized in Section 6. We use a standard Λ cold dark matter cosmology throughout this paper, with $\Omega_\Lambda = 0.7$, $\Omega_M = 0.3$, and $H_0 = 70\,\mathrm{km\,s^{-1}\,Mpc^{-1}} \equiv 100\,h\,\mathrm{km\,s^{-1}Mpc^{-1}}$. The function $E(z)$ arises in the evolution of the scaling relations and describes the evolution of the Hubble parameter. It is given by $E(z) = \sqrt{\Omega_M(1+z)^3 + \Omega_\Lambda}$.

2 DATA ANALYSIS

2.1 Sample selection

The sample used in this work is a subset of 23 low-mass clusters or groups from the 400 d survey. The 400 d survey (Burenin et al. 2007) is an extension of 160 d *ROSAT* Position Sensitive Proportional Counter (PSPC) survey (Vikhlinin et al. 1998), and is based on 1610 pointings covering an area of 397 deg^2, using the same detection algorithm as the 160 d survey. Observations of the evolution of the clusters were used to place tight constraints on cosmological parameters (Vikhlinin et al. 2009a,b). Our subsample is complete above a flux limit of 5×10^{-13} erg s^{-1} cm^{-2}, and within a redshift range $0.03 < z < 0.15$. The flux limit is defined in the observer's frame 0.5–2 keV energy band from the *ROSAT* observations. The clusters have all been re-observed with *Chandra*, and the details of the *Chandra* observations are provided in Table 1. Fig. 1 shows the luminosity–redshift distribution in the 400 d survey, and highlights the subsample used for this work. The sample comprises galaxy groups and low-mass clusters, with a median temperature of $\sim$2 keV, and for convenience it is referred to as the 400 d groups sample.

2.2 Data reduction and analysis

The *Chandra* observations of the clusters were reduced and analysed using CIAO (Fruscione et al. 2006) version 4.6.1. The data

Table 1. Summary of the 400 d groups sample and the *Chandra* data used. RA and Dec. and redshift information are from Burenin et al. (2007). The *Chandra* observation ID and detector (ACIS-I or ACIS-S) are given, along with the cleaned exposure time of the *Chandra* observation. Column 8 gives a number indicating the paper presenting the original analysis of the observations (where available) as follows: (1) Sun (2009); (2) Sun et al. (2009); (3) Ma et al. (2011); (4) Hofmann et al. (2016); (5) Vikhlinin et al. (2005); (6) Khosroshahi, Ponman & Jones (2007).

Clusters	RA	Dec.	Redshift	Observation ID	ACIS-I/S	Exposure (ks)	PI	Reference
Cl0327+0233	03:27:54.5	+02:33:47	0.030	9391	I	11.12	Vikhlinin	1
Cl0306−0943	03:06:28.7	−09:43:50	0.034	9389	I	10.05	Vikhlinin	1
Cl1058+0136	10:58:12.6	+01:36:58	0.038	9387	I	10.05	Vikhlinin	2
Cl1259+3120	12:59:51:0	+31:20:48	0.052	9395	I	17.92	Vikhlinin	1
Cl0334−3900	03:34:03.3	−39:00:46	0.062	9393	I	15.56	Vikhlinin	1
Cl0810+4216	08:10:24.2	+42:16:19	0.064	13986	I	9.95	Maughan	
Cl1630+2434	16:30:14.7	+24:34:47	0.065	9386	I	9.65	Vikhlinin	
Cl1533+3108	15:33:17.1	+31:08:55	0.067	9384	I	9.99	Vikhlinin	2
Cl0340−2840	03:40:27.2	−28:40:20	0.068	9385	I	9.64	Vikhlinin	
Cl1206−0744	12:06:33.5	−07:44:24	0.068	9388	I	10.01	Vikhlinin	2
A1775	13:41:52.0	+26:22:49	0.076	12891	S	39.52	Hofmann	4
–	–	–	–	13510	S	59.26	Hofmann	4
A744	09:07:20.0	+16:39:25	0.076	6947	I	39.52	Vikhlinin	2
RXJ1159+5531	11:59:51.2	+55:31:56	0.081	4964	S	75.11	Vikhlinin	5
Cl2220−5228	22:20:09.1	−52:28:01	0.102	9383	I	10.04	Vikhlinin	
Cl0336−2804	03:36:49.4	−28:04:53	0.104	9390	I	10.63	Vikhlinin	3
Cl1501−0830	15:01:18.3	−08:30:33	0.108	13987	I	9.94	Maughan	
A2220	16:39:55.5	+53:47:55	0.111	7876	S	14.95	Jetha	1
–	–	–	–	9832	S	18.81	Jetha	1
Cl0057−2616	00:57:24.7	−26:16:49	0.113	9427	I	9.99	Vikhlinin	3
Cl0838+1948	08:38:31.4	+19:48:15	0.123	9397	I	19.97	Vikhlinin	3
Cl0237−5224	02:37:59.6	−52:24:47	0.134	9392	I	13.95	Vikhlinin	
Cl1552+2013	15:52:12.3	+20:13:42	0.136	3214	S	14.93	Jones	6
RXJ1416.4+2315	14:16:26.8	+23:15:30	0.138	2024	S	14.57	Jones	6
Cl0245+0936	02:45:45.7	+09:36:36	0.147	9394	I	14.97	Vikhlinin	3

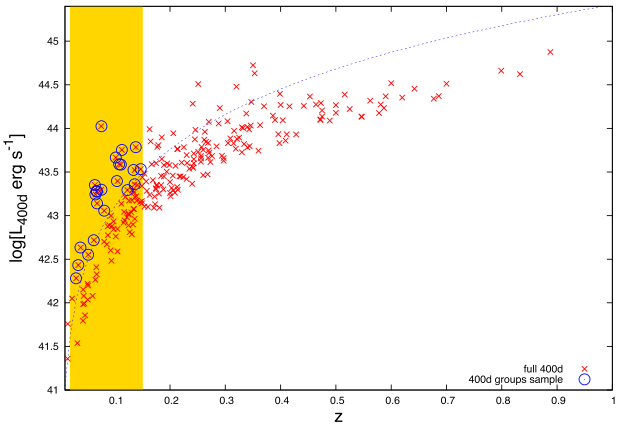

Figure 1. Distribution of the 400 d clusters in the luminosity–redshift plane. Red crosses show the full 400 d survey, blue circles within the golden box show the 400 d groups sample studied in this work, with the gold box highlighting the $0.03 < z < 0.15$ range used to select the clusters. The blue dashed line give the flux limit of the 400 d groups sample of 5×10^{-13} erg s^{-1} cm^{-2}.

were reprocessed from level 1 events using the *Chandra* calibration data base (Fruscione et al. 2006) version 4.6.1, and the normal data cleaning and reduction steps were followed. In particular, background light curves were produced and cleaned to remove periods of high background in a manner consistent with the blank-sky background data sets, which were subsequently used to estimate the background for our spectral analyses. Most of the clusters in this work were observed in VFAINT mode, so the additional VFAINT cleaning process was applied where appropriate.

After this data reduction, the properties of the clusters were measured following the methods described in Maughan et al. (2012), and we recap the key points here. Gas masses were measured by fitting a projected model of the gas density profile to the observed profile of the projected emissivity. The gas temperature and luminosity were measured from spectra extracted within R_{500} (the radius within which the overdensity is 500 times the critical density at the cluster redshift). The value of R_{500} was determined iteratively from the Y_X–M_{500} scaling relation of Vikhlinin et al. (2009a)

$$M_{500} = E(z)^{-2/5} A_{YM} \left(\frac{Y_X}{3 \times 10^{14}\,\mathrm{M}_\odot \mathrm{keV}} \right)^{B_{YM}}, \quad (1)$$

where the Y_X is the product of temperature (measured with the central 15 per cent of R_{500} excluded) and gas mass, $A_{YM} = 5.77 \times 10^{14} h^{1/2}\,\mathrm{M}_\odot$, $B_{YM} = 0.57$.

For all analyses, the blank-sky background files were used to estimate the background level at the cluster position. For the imaging analysis, which was performed in the 0.7−2 keV band, the background was normalized to match the count rate in parts of the cluster field that were free from source emission. For the spectral analysis, the exposure time of the blank-sky files was adjusted so their count rates matched those of the cluster data in the 9.5−12 keV band. A residual spectrum was produced by subtracting a background-field spectrum from a source-field spectrum in a region free from source emission. This residual spectrum was fit with an unabsorbed APEC (Smith et al. 2001) model with $T = 0.18$ keV, which was included as an extra component in all subsequent spectral fits to the cluster spectra (see Vikhlinin et al. 2005).

Table 2. Cluster properties measured in the $(0-1)R_{500}$ aperture. $L_{\rm tot}$ and L_{52} are the *Chandra* luminosities in the bolometric and soft (0.5−2 keV) band. $L_{400\,\rm d}$ is the *ROSAT* PSPC luminosity in the same soft band from Burenin et al. (2007); unlike the properties measured with *Chandra* this is the total luminosity of the cluster, not the luminosity within R_{500}.

Cluster	z	R_{500} (Mpc)	$T_{\rm tot}$ (keV)	$L_{\rm tot}$ (10^{43} erg s^{-1})	L_{52} (10^{43} erg s^{-1})	$L_{400\,\rm d}$ (10^{43} erg s^{-1})
Cl0327+0233	0.030	0.374	$0.98^{+0.04}_{-0.04}$	0.36 ± 0.02	0.20 ± 0.01	0.19 ± 0.02
Cl0306−0943	0.034	0.411	$1.15^{+0.06}_{-0.07}$	0.68 ± 0.08	0.37 ± 0.05	0.27 ± 0.03
Cl1058+0136	0.038	0.559	$2.30^{+0.29}_{-0.25}$	10.70 ± 0.90	0.56 ± 0.05	0.43 ± 0.06
Cl1259+3120	0.052	0.416	$1.05^{+0.11}_{-0.08}$	0.55 ± 0.85	0.29 ± 0.04	0.36 ± 0.10
Cl0334−3900	0.062	0.666	$2.53^{+0.59}_{-0.46}$	2.01 ± 0.18	0.83 ± 0.07	0.58 ± 0.04
Cl0810+4216	0.064	0.777	$3.51^{+0.41}_{-0.50}$	6.63 ± 0.43	2.86 ± 0.16	2.24 ± 0.25
Cl1630+2434	0.065	0.730	$2.86^{+0.44}_{-0.43}$	5.10 ± 0.43	2.09 ± 0.18	1.75 ± 0.25
Cl1533+3108	0.067	0.608	$1.67^{+0.12}_{-0.11}$	3.35 ± 0.26	1.66 ± 0.13	1.90 ± 0.31
Cl0340−2840	0.068	0.662	$2.13^{+0.53}_{-0.20}$	3.28 ± 0.32	1.47 ± 0.14	1.90 ± 0.37
Cl1206−0744	0.068	0.638	$1.73^{+0.22}_{-0.05}$	3.66 ± 0.27	1.78 ± 0.13	1.38 ± 0.16
A1775	0.076	0.962	$3.89^{+0.09}_{-0.09}$	25.64 ± 0.16	9.29 ± 0.58	10.60 ± 1.09
A744	0.076	0.682	$2.45^{+0.19}_{-0.20}$	5.02 ± 0.29	2.21 ± 0.86	1.98 ± 0.22
RXJ1159+5531	0.081	0.617	$1.68^{+0.02}_{-0.02}$	2.74 ± 0.07	1.43 ± 0.04	1.14 ± 0.12
Cl2220−5228	0.102	0.890	$3.79^{+0.48}_{-0.48}$	15.11 ± 0.81	5.48 ± 0.59	4.64 ± 0.55
Cl0336−2804	0.104	0.661	$2.06^{+0.43}_{-0.28}$	4.44 ± 0.48	2.02 ± 0.22	2.49 ± 0.44
Cl1501−0830	0.108	0.745	$1.93^{+0.14}_{-0.33}$	13.62 ± 0.95	6.49 ± 0.45	3.88 ± 0.49
A2220	0.111	0.727	$2.67^{+0.35}_{-0.27}$	7.58 ± 0.35	3.20 ± 0.15	3.83 ± 0.42
Cl0057−2616	0.113	0.812	$2.56^{+0.40}_{-0.25}$	13.42 ± 0.86	5.70 ± 0.36	5.66 ± 0.68
Cl0838+1948	0.123	0.738	$3.11^{+0.60}_{-0.59}$	5.73 ± 0.59	2.26 ± 0.23	1.96 ± 0.50
Cl0237−5224	0.134	0.703	$2.45^{+0.38}_{-0.36}$	7.48 ± 0.69	3.27 ± 0.30	3.33 ± 0.35
Cl1552+2013	0.136	0.603	$2.52^{+0.67}_{-0.31}$	5.12 ± 0.33	2.19 ± 0.14	2.29 ± 0.28
RXJ1416.4+2315	0.138	0.623	$2.97^{+0.37}_{-0.37}$	11.28 ± 0.47	5.33 ± 0.22	6.09 ± 0.64
Cl0245+0936	0.147	0.667	$2.36^{+0.44}_{-0.44}$	4.74 ± 0.80	2.19 ± 0.37	3.41 ± 1.10

Luminosities and temperatures were measured within R_{500} both with and without the central $0.15R_{500}$ of the aperture being included. Luminosities were measured in the bolometric band and the (0.5−2) keV band. All luminosities are unabsorbed, measured in the cluster rest frame, and are projected luminosities (i.e. not corrected for the fact that emission beyond R_{500} is projected on to the cluster, or that the exclusion of the central projected $0.15R_{500}$ also excludes emission outside that 3D radius along the line of sight). We use the notation that $T_{\rm tot}$ and $T_{\rm ce}$ refer to temperatures measured in the R_{500} and $(0.15–1)R_{500}$ apertures, respectively, and $L_{\rm tot}$ and $L_{\rm ce}$ refer to bolometric (0.01−100 keV) luminosities in the same apertures. We use L_{52} to denote the soft-band (0.5−2 keV) luminosity in the R_{500} aperture. Finally, we use $L_{400\,\rm d}$ to denote the soft-band (0.5−2 keV) luminosity measured with the *ROSAT* PSPC in the original 400 d survey data (all other luminosities were measured with *Chandra*). The properties of the clusters are summarized in Tables 2 and 3.

To assess the dynamical state and presence of any CCs for this sample, we use the cuspiness of the ICM density profile, the core flux ratio $F_{\rm core}$, and a visual classification of the X-ray morphology to categorize clusters. Cuspiness is defined as the logarithmic slope of the gas density profile at $0.04R_{500}$, which was measured from our 3D gas density model. $F_{\rm core}$ is defined as the ratio of the unabsorbed bolometric flux within the $0.15R_{500}$ aperture to the total flux in the R_{500} region. A cluster was categorized as a CC cluster if it had a cuspiness >0.7 and $F_{\rm core} > 0.3$ (6/23 clusters). Clusters were classed as being relaxed if the X-ray images were smooth and symmetric, without secondary peaks or other substructures (12/23 clusters). With these measurements, we defined a sample of five relaxed cool-core clusters (RCC) as being those relaxed clusters that were also CC clusters. The other 18 clusters were classed as non-relaxed-cool-core (NRCC; i.e. the complement of the RCC set). The dynamical properties of each cluster are summarized in Table 4.

2.3 Notes on individual groups

In some instances the luminosity of a group measured with *Chandra* significantly differed from that measured with *ROSAT*. Some variation is expected due to differences in calibration and apertures, and is modelled with a nuisance parameter in our Bayesian analysis. In this section, we discuss groups where the difference in flux is significant, or where non-standard steps were required in our analysis.

Cl0334−3900: this group has an irregular morphology and was classified as a multiple component system by the 400 d detection algorithm. The value of $L_{400\,\rm d}$ in Table 2 is for the main component. For the *Chandra* analysis, we included all of the flux within R_{500} of the main component, resulting in a higher flux. When the fluxes from all components in the 400 d catalogue are combined, the *Chandra* and 400 d fluxes agree well. The use of the 400 d flux of the main component alone is consistent with the 400 d selection function, but in fact the detection probability for this group is $\approx$1 whichever flux is used so the choice makes no practical difference in our analysis.

Table 3. Cluster properties measured in the $(0.15-1)R_{500}$ aperture. L_{ce} is the *Chandra* bolometric luminosity.

Cluster	z	T_{ce} (keV)	L_{ce} (10^{43} erg s^{-1})
Cl0327+0233	0.030	$0.92^{+0.07}_{-0.10}$	0.18 ± 0.02
Cl0306−0943	0.034	$1.19^{+0.11}_{-0.12}$	0.28 ± 0.07
Cl1058+0136	0.038	$2.33^{+0.30}_{-0.26}$	9.80 ± 0.88
Cl1259+3120	0.052	$1.00^{+0.07}_{-0.11}$	0.42 ± 0.10
Cl0334−3900	0.062	$2.56^{+0.73}_{-0.52}$	1.76 ± 0.17
Cl0810+4216	0.064	$3.67^{+0.60}_{-0.73}$	4.04 ± 0.38
Cl1630+2434	0.065	$2.55^{+0.52}_{-0.38}$	4.06 ± 0.39
Cl1533+3108	0.067	$1.52^{+0.17}_{-0.23}$	2.66 ± 0.36
Cl0340−2840	0.068	$2.09^{+0.45}_{-0.26}$	2.66 ± 0.29
Cl1206−0744	0.068	$1.72^{+0.14}_{-0.10}$	2.88 ± 0.23
A1775	0.072	$3.65^{+0.13}_{-0.14}$	16.60 ± 0.14
A744	0.076	$2.17^{+0.28}_{-0.16}$	3.14 ± 0.16
RXJ1159+5531	0.081	$1.72^{+0.10}_{-0.04}$	1.46 ± 0.06
Cl2220−5228	0.102	$3.32^{+0.48}_{-0.44}$	11.78 ± 0.77
Cl0336−2804	0.104	$1.86^{+0.29}_{-0.34}$	3.68 ± 0.47
Cl1501−0830	0.108	$1.91^{+0.14}_{-0.33}$	13.14 ± 0.93
A2220	0.111	$2.62^{+0.34}_{-0.30}$	6.59 ± 0.33
Cl0057−2616	0.113	$2.37^{+0.30}_{-0.34}$	10.10 ± 0.80
Cl0838+1948	0.123	$3.26^{+0.82}_{-0.85}$	3.79 ± 0.64
Cl0237−5224	0.134	$2.04^{+0.45}_{-0.32}$	5.85 ± 0.71
Cl1552+2013	0.136	$2.57^{+0.91}_{-0.32}$	4.75 ± 0.51
RXJ1416.4+2315	0.138	$2.72^{+0.35}_{-0.35}$	8.13 ± 0.44
Cl0245+0936	0.147	$2.09^{+0.64}_{-0.35}$	3.45 ± 0.70

Table 4. Dynamical properties and classification of the clusters.

Cluster	Relaxed	F_{core}	cuspiness	CC	RCC
Cl0327+0233		0.44	1.02	√	
Cl0306−0943	√	0.59	1.54	√	√
Cl1058+0136		0.23	0.70		
Cl1259+3120	√	0.24	0.49		
Cl0334−3900		0.12	0.55		
Cl0810+4216	√	0.39	0.89	√	√
Cl1630+2434	√	0.20	0.70		
Cl1533+3108	√	0.21	0.26		
Cl0340−2840		0.19	0.49		
Cl1206−0744		0.21	0.94		
A1775		0.35	0.66		
A744	√	0.37	0.74	√	√
RXJ1159+5531	√	0.45	1.31	√	√
Cl2220−5228	√	0.22	0.54		
Cl0336−2804		0.17	0.41		
Cl1501−0830		0.04	0.01		
A2220		0.09	0.87		
Cl0057−2616	√	0.25	0.49		
Cl0838+1948	√	0.34	0.81	√	√
Cl0237−5224		0.22	0.51		
Cl1552+2013		0.05	0.76		
RXJ1416.4+2315	√	0.63	–		
Cl0245+0936	√	0.27	0.93		

Cl1501−0830: this group also has an irregular morphology, with a clump to the south-west that was excluded in the 400 d analysis due to its proximity to a bright point source. The point source is resolved and excluded in the *Chandra* analysis allowing both components of the group to be included in the *Chandra* flux. The exclusion of the south-west clump in the 400 d flux has negligible impact on our results since the 400 d detection probability of the group is ≈1 regardless, and the difference between the *Chandra* and 400 d fluxes is absorbed in our nuisance parameter.

A2220: part of the emission from this system extended off the *Chandra* Advanced CCD Imaging Spectrometer (ACIS-S) array. In our standard analysis, any flux missing in an aperture due to excised sources or chip gas is corrected by assuming azimuthal symmetry of the X-ray surface brightness profile. In the case of A2220, this was not appropriate as the emission was significantly elongated in the direction towards the chip gap (meaning an azimuthal average would underestimate the missing flux). In this case, the missing flux was corrected by scaling for the off-chip regions using the flux distribution in the *ROSAT* image. This increased the *Chandra* flux by ≈40 per cent.

RXJ1416.4+2315: the observation of this group exhibited background flares throughout, and so an extra power-law component was included when modelling the residual spectrum, as described in the appendix.

3 THE *L–T* RELATION WITHOUT BIAS CORRECTIONS

In this section, we present the bolometric *L–T* relation for the 400 d groups sample, without accounting for any selection biases.

The correlation between L and T arises in the self-similar model due to the way that the gas mass, temperature and cluster structural parameters all scale with mass, with an additional assumption that the luminosity is dominated by bremsstrahlung emission (see Maughan 2014, for an expanded discussion). This gives rise to the expectation of a self-similar bolometric *L–T* relation of the form $L \propto T^2$. For cooler clusters where line emission becomes comparable to the bremsstrahlung component, the slope should flatten.

To measure the *L–T* relation, our data were fit with a power-law model of the form

$$\frac{L}{L_0} = E(z)^{\gamma_{LT}} A_{LT} \left(\frac{T}{T_0}\right)^{B_{LT}}. \quad (2)$$

For all of our fits, we used $L_0 = 1.0 \times 10^{43}$ergs^{-1}, $T_0 = 2.0$ keV, and fixed $\gamma_{LT} = 1$ (for self-similar evolution – a negligible assumption for the redshift range covered here).

For the purposes of comparison with other work, and to assess the size of the sample selection biases, the *L–T* relation was first measured without modelling the selection biases. The *L–T* data were fit in base-10 log space using bivariate, correlate errors and scatter (BCES) orthogonal linear regression following Akritas & Bershady (1996). The intrinsic scatter of the *L–T* relation (δ_{LT}) was measured by determining the additional error component needed to give a reduced χ^2 of unity, as in Maughan (2007).

The relation was fit for the different apertures used to measure L and T, and the best-fitting relations are summarized in Table 5. In both cases, the slope of the *L–T* relation is significantly steeper than the self-similar expectation of $B_{LT} = 2$.

We compared the *L–T* relation for this sample with the previously published relations of Pratt et al. (2009, hereafter P09), which comprised 31 low-z clusters from the Representative XMM-Newton Cluster Structure Survey (REXCESS) sample with

Table 5. *L–T* relation parameters for the 400 d groups sample without corrections for selection biases. Best-fitting parameters are given for the whole sample of 23 clusters, and the subsamples of RCC (five clusters) and NRCC systems (18 clusters). Luminosities are bolometric, and the relations are given for properties measured with core regions included and excised for each subsample. The scatter, δ_{LT} is given as a fractional value.

Parameters	All		RCC		NRCC	
	$(0.15-1)R_{500}$	$(0-1)R_{500}$	$(0.15-1)R_{500}$	$(0-1)R_{500}$	$(0.15-1)R_{500}$	$(0-)R_{500}$
A_{LT}	2.52 ± 0.45	3.18 ± 0.42	1.39 ± 0.28	2.51 ± 0.26	3.08 ± 0.56	3.42 ± 0.57
B_{LT}	3.81 ± 0.46	3.28 ± 0.33	2.59 ± 0.37	2.15 ± 0.17	3.85 ± 0.52	3.49 ± 0.41
δ_{LT}	0.59 ± 0.17	0.47 ± 0.11	0.46 ± 0.19	0.18 ± 0.01	0.52 ± 0.13	0.49 ± 0.15

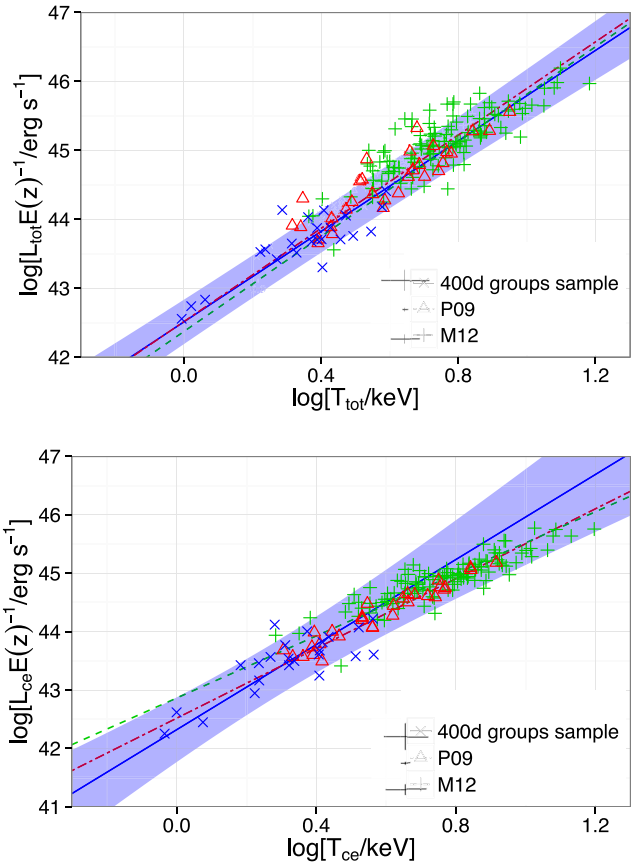

Figure 2. The *L–T* relation (without bias correction) for the 400 d groups sample (blue crosses, blue solid line with shaded error region) is compared with the REXCESS clusters from P09 (red triangles and red dot–dashed line), and the archival *Chandra* sample of M12 (green plus symbols and green dashed line). Top: quantities measured within the $(0-1)R_{500}$ aperture. Bottom: quantities measured within the $(0.15-1)R_{500}$ aperture. In both plots, the legend shows representative error bars for the samples.

XMM–Newton data, and Maughan et al. (2012, hereafter M12), containing 114 clusters over $0.1 < z < 1.1$ with *Chandra* data analysed consistently with this work. These comparisons are shown in Fig. 2 and for the moment we simply note the good agreement of the new 400 d *L–T* relation with the samples of more massive systems.

Some caution should be applied with comparing the *L–T* relation of the P09 data with those of the 400 d groups and M12 samples, as the P09 measurements were based on *XMM–Newton* data while the other two samples used *Chandra* data. There is a significant offset between the temperatures measured with the two observatories, with the *XMM–Newton* temperature being systematically lower than those measured with *Chandra* (Schellenberger et al. 2015). However the difference decreases at lower temperatures and is $<\sim$10 per cent below 4 keV so does not strongly impact the comparison between distributions of the data points in that regime.

One notable difference between the 400 d groups sample and those of P09 and M12 is that unlike the other two samples, the 400 d groups and low-mass clusters show no evidence for a reduction in the intrinsic scatter of the *L–T* relation when the core regions are removed. Furthermore, the scatter in the 400 d sample with core regions excised is significantly larger than the equivalent scatter in the P09 and M12 samples. This demonstrates that, while the scatter in the more massive clusters sampled by P09 and particularly M12 is driven by the core regions, this is not the case for the lower mass systems in our 400 d sample. We investigated whether the scatter in the 400 d groups sample had an origin in the dynamical state of the objects by fitting the *L–T* relation to the subsamples of visually classified relaxed and unrelaxed clusters. The sample sizes (12 for relaxed and 11 for unrelaxed subsamples) were not large enough to allow precise measurements and while the scatter for the unrelaxed clusters (0.51 ± 0.27) was larger than the relaxed clusters (0.66 ± 0.12), the difference was not significant.

4 THE *L–T* RELATION WITH BIAS CORRECTION

The preceding analysis did not take into account selection effects induced by the use of an X-ray-selected sample of clusters. However, the fact that the 400 d groups sample is complete, with a well-defined selection function means that selection effects can be incorporated into the analysis. To do this, we use a Bayesian approach and computed the likelihood of the observed properties of the sample for a model which comprises the cluster temperature function, the *L–T* relation (parametrized by A_{LT} and B_{LT}; γ_{LT} was fixed at the self-similar value), its intrinsic scatter (δ_{LT}, modelled as lognormal) and the sample selection function (which contains a parameter X_{cal}, defined below, to model systematic differences between *ROSAT* and *Chandra*).

4.1 The likelihood

We use an improved version of the likelihood model of Pacaud et al. (2007, presented in detail in Pacaud et al. 2016). The likelihood starts with the probability of a cluster in the survey volume having some temperature T. This is given by a mass function (we used Tinker et al. 2008) converted to a temperature function $\phi(T, z)$ by assuming a fixed mass–temperature ($M–T$) relation (we use the bias-corrected relation of Kettula et al. 2015, which was calibrated to *Chandra* temperatures). Then, the probability of a cluster with temperature T having some luminosity L is given by the model *L–T* relation including its scatter, $P(L|T, z, \theta)$ [where θ is our set of model parameters]. In order to apply the selection function,

soft-band luminosities are used throughout, and the selection probability $P(I|L, z)$ is applied to the clusters based on their $L_{400\,\mathrm{d}}$. Finally, the likelihood of the observations is computed using their measurement errors, including the original 400 d luminosity, and the luminosity and temperature measured in the *Chandra* observations (here we include a nuisance parameter, $X_{\mathrm{cal}} \equiv L_{52}/L_{400\,\mathrm{d}}$ to describe any systematic differences between the 400 d and *Chandra* luminosities).

The likelihood for cluster i is then

$$P(\hat{L}_{400\mathrm{d},i}, \hat{L}_{52,i}, \hat{T}_i|z_i, \theta) = \int \mathrm{d}T \int \mathrm{d}L_{400\mathrm{d}}\, P(T|z_i)$$
$$\times P(L_{400\mathrm{d}}|T, z_i, \theta)\, P(\hat{L}_{400\mathrm{d},i}|L_{400\mathrm{d}})$$
$$\times P(\hat{L}_{52,i}|L_{400\mathrm{d}}, X_{\mathrm{cal}})\, P(\hat{T}_i|T)\, P(I|L_{400\mathrm{d}}, \hat{L}_{400\mathrm{d},i}, z_i), \quad (3)$$

where hats indicate observed quantities (we neglect measurement errors on z, so $z \equiv \hat{z}$).

$P(T|z_i)$ is the prior probability that a cluster at redshift z_i would have a temperature T, and is given by the normalized temperature function:

$$P(T|z_i) = \frac{\Phi(T, z_i)}{\int \mathrm{d}T\, \Phi(T, z_i)}. \quad (4)$$

The selection function $P(I|L_{400\mathrm{d}}, \hat{L}_{400\mathrm{d},i}, z_i)$ is composed of two terms: the full 400 d selection function (denoted P_1), and the flux cut used to define the 400 d groups sample (denoted P_2). P_1 depends on the nominal 'true' 400 d flux and not the measured flux, because the scatter between the 'true' and measured flux is modelled in the selection function (Burenin et al. 2007). The flux cut P_2 however, is applied to the measured fluxes, so the selection function can be written

$$P(I|L_{400\mathrm{d}}, \hat{L}_{400\mathrm{d},i}, z_i) = P_1(I|L_{400\mathrm{d}}, z_i)\, P_2(I|\hat{L}_{400\mathrm{d},i}, z_i). \quad (5)$$

The probability in equation (3) must be normalized, and this is done by dividing it by its integral over the whole observable part of the L, T plane, which we write as

$$C_i = \int \mathrm{d}\hat{T} \int \mathrm{d}\hat{L}_{400\mathrm{d}} \int \mathrm{d}\hat{L}_{52}\, P(\hat{L}_{400\mathrm{d},i}, \hat{L}_{52,i}, \hat{T}_i|z_i, \theta). \quad (6)$$

The final likelihood of the sample is then the product of this normalized probability over all clusters:

$$\mathcal{L}(\hat{L}_{400\mathrm{d}}, \hat{L}_{52}, \hat{T}|z, \theta) = \prod_i^{N_{\mathrm{det}}} \frac{P_i(\hat{L}_{400\mathrm{d},i}, \hat{L}_{52,i}, \hat{T}_i, |z_i, \theta)}{C_i}. \quad (7)$$

4.2 Implementation

The likelihood function was multiplied by the prior probability distributions of the parameters. These were uniform for A_{LT}, B_{LT} and δ_{LT}, while the prior on X_{cal} was lognormal centred on $\log(X_{\mathrm{cal}}) = 0$ with a standard deviation of 0.5 in natural log space. The posterior was then sampled using Markov Chain Monte Carlo (MCMC) with LAPLACES DEMON[1] in R (R Core Team 2014). Three independent MCMC chains were run, and we checked that they had converged after any non-stationary parts had been discarded from the starts of the chains. The parameters posterior distributions were then computed from the combined chain and are reported here as the mean and standard deviation of the posterior samples.

[1] https://github.com/ecbrown/LaplacesDemon (Statisticat LLC 2016).

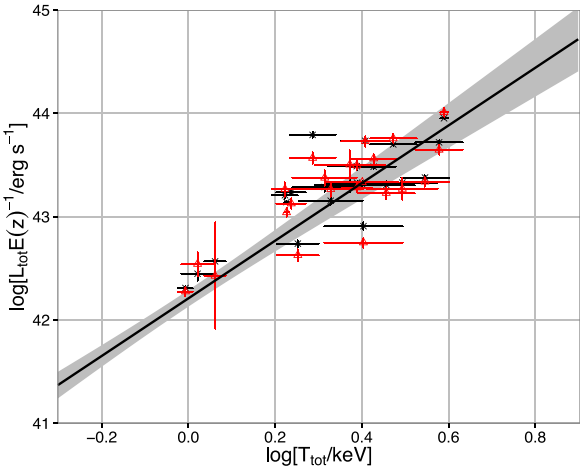

Figure 3. Bias-corrected *L–T* relation. The black crosses are the observed *Chandra* luminosities, while the red triangles show the original 400 d *ROSAT* luminosities (all the luminosities are in the (0.5−2) keV energy band with the core regions included). The temperature for each point is the *Chandra* temperature from this work.

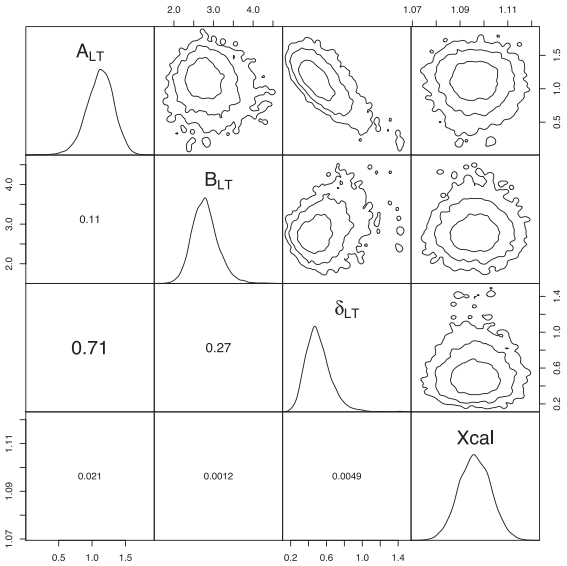

Figure 4. Correlation matrix of the bias-corrected *L–T* model parameters. The contours shown above the diagonal are 1σ, 2σ and 3σ confidence contours for the parameter posterior densities along the diagonal. The values below the diagonal are the magnitude of Pearson's correlation coefficient for the corresponding pair of parameters, with a font size proportional to the strength of correlation.

4.3 Results of bias-corrected *L–T* fit

The method described in the preceding sections was used to estimate the *L–T* relation of the 400 d groups sample, including the effects of selection biases. For these results, we assumed the *M–T* relation of Kettula et al. (2015, choosing the relation that was bias-corrected and calibrated to *Chandra* temperatures); we test the sensitivity of our results to this assumption later in Section 5.1. The best-fitting bias-corrected relation is shown in Fig. 3, with $\boldsymbol{A}_{\mathrm{LT}} = 1.12 \pm 0.21$, $\boldsymbol{B}_{\mathrm{LT}} = 2.79 \pm 0.33$, $\boldsymbol{\delta}_{\mathrm{LT}} = 0.51 \pm 0.15$ and $\boldsymbol{X}_{\mathrm{cal}} = 1.10 \pm 0.01$. The parameter posterior distributions are shown in Fig. 4, and are summarized in Table 6.

Table 6. Best-fitting parameters for the (0.5−2) keV band, core-included *L–T* relation, including correction for selection biases. The columns show the impact of the choice of *M–T* relation used in the analysis. The first column shows our main results, using the *M–T* relation from Kettula et al. (2015, K14). We also show the results for the *M–T* relations of Sun et al. (2009, S09) and Finoguenov, Reiprich & Böhringer (2001, F01).

M–T	K14	S09	F01
$A_{\rm LT}$	1.12 ± 0.21	1.10 ± 0.21	1.11 ± 0.25
$B_{\rm LT}$	2.79 ± 0.33	2.85 ± 0.33	3.00 ± 0.35
$\delta_{\rm LT}$	0.51 ± 0.15	0.50 ± 0.15	0.53 ± 0.15
$X_{\rm cal}$	1.10 ± 0.01	1.10 ± 0.01	1.10 ± 0.01

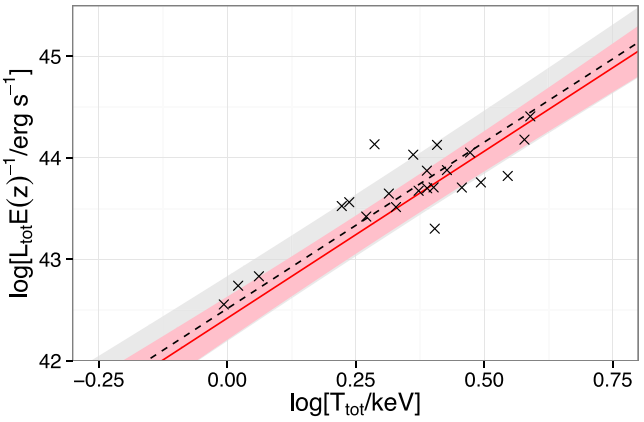

Figure 5. Bolometric, core-included *L–T* relations of the 400 d groups sample with and without bias correction. The black dashed line with slightly higher normalization and grey-shaded error region is the relation without bias correction. The red solid line with pink-shaded error region is the bias-corrected model.

Recall that for the bias-corrected fit, we use the soft-band luminosities in the $(0-1)R_{500}$ aperture. In order to compare this fit with the more widely used bolometric *L–T* relations, we converted the bias-corrected soft-band *L–T* relation into a bolometric *L–T* relation by applying a bolometric correction of the form

$$\frac{L_{\rm bol}}{L_{0.5-2}} = 2.3 \left(\frac{T}{2}\right)^{0.50}. \quad (8)$$

This was determined by generating model APEC spectra in XSPEC (Arnaud 1996) and computing the ratios of the fluxes in the 0−100 keV and 0.5−2 keV energy bands for models with different temperatures. The ratios as a function of temperature were fit with a BCES regression in log space to give the power-law parameters. The resulting bias-corrected estimate of the bolometric *L–T* relation is plotted in Fig. 5 along with the original bolometric *L–T* relation we measured in Section 3 without correcting for biases. The bias-corrected bolometric normalization was $A_{\rm LT} = 2.58 \pm 0.21$ and the slope was 3.29 ± 0.33. As expected, the bias correction reduces the normalization of the bolometric *L–T* relation, but the size of the effect is small. Neither the slope or scatter of the *L–T* relation are significantly altered by our bias correction, indicating that the 400 d groups sample is not strongly affected by Malmquist and Eddington biases.

We also measured the *L–T* relation using the core-excised temperatures, and the best-fitting bias-corrected relation was not significantly changed. This is consistent with our observation that the sample does not contain a significant number of strong CC clusters. We proceed with the results based on temperatures measured with the core regions included due to the improved statistical precision on the measured temperatures.

As an aside, we note that the absence of strong CC clusters in the 400 d groups sample is unlikely to be due to them being rejected by the 400 d determined algorithm. Our simulations have shown that strong CC clusters are efficiently recovered by the 400 d detection algorithm even to high redshifts (Burenin et al. 2007; Vikhlinin et al. 2007).

5 DISCUSSION

5.1 Impact of the assumed *M–T* relation

A significant step in our model for the likelihood of the *L–T* observations is the conversion of the theoretical mass function to a temperature function by way of an assumed *M–T* relation. For our main analysis, we assumed the recent *M–T* relation of Kettula et al. (2015), which is calibrated with weak lensing masses, and covers a range of masses from groups up to clusters. We investigated the sensitivity of our results to this choice by applying two alternate *M–T* relations from Sun et al. (2009) and Finoguenov et al. (2001). The best-fitting parameters of the *L–T* relation for the different choices of *M–T* relation are shown in Table 6. It is clear that the choice of *M–T* relation has no significant impact on our inference of the *L–T* relation parameters.

Our analysis also makes the simplifying assumption that there is no scatter in the *M–T* relation. For cosmological analyses based on cluster number counts, neglecting this scatter can introduce significant biases (e.g. Sahlén et al. 2009). For our likelihood model for the *L–T* relation, the effect should be smaller. To first order, marginalizing over scatter in the *M–T* relation would have the effect of smoothing the temperature function in the likelihood. This would flatten the temperature function somewhat, reducing the level of the Eddington bias in a sample. Any neglected mass-dependence of the *M–T* scatter would also influence our measurement of the slope of the *L–T* relation. Given that the amount of bias in our sample is small (e.g. Fig. 5), we estimate that the impact of neglecting the scatter is small, but this remains a systematic uncertainty in our analysis.

5.2 The slope of the *L–T* relation

Our analysis of the 400 d groups sample is one of several recent studies to look at the *L–T* relation of low-mass systems that have accounted for biases. By compiling our results with those other recent studies, we can build a reliable picture of the nature of the *L–T* relation in the group regime. In particular we focus on the slope of the *L–T* relation, which is a diagnostic of feedback processes in the ICM.

L14 analysed a sample of 20 groups with *XMM–Newton* data, which was statistically complete, allowing the selection bias effects to be included in the analysis. Their bias correction was determined by sampling populations of clusters from a mass function, and assigning luminosities and temperatures from a combination of luminosity–mass (*L–M*) and *L–T* scaling relations. Their selection function was then applied and the scaling relations were fit to the simulated samples to find the input *L–M* and *L–T* relations that produced the best agreement with the observed scaling relations. The *L–T* fits were performed using BCES *Y*|*X* regression, giving a slope

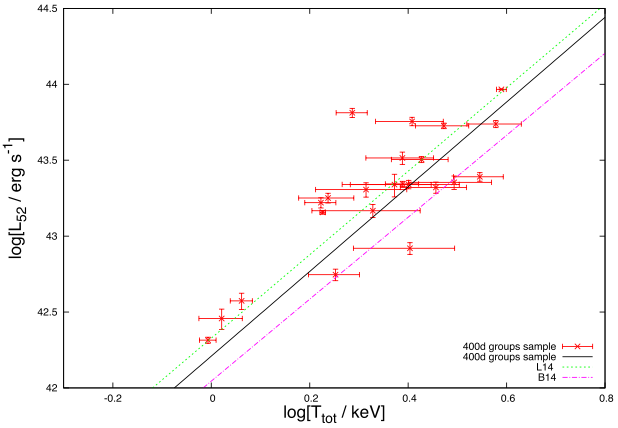

Figure 6. The 400 d groups bias-corrected *L–T* relation is compared with the bias-corrected fits from L14 and B14.

of $B_{\rm LT} = 2.05 \pm 0.32$ which increased to 2.86 ± 0.29 when the bias correction was applied. We note that the slopes for their *L–T* relation without bias correction range from 2.05–2.76 depending on the type of BCES regression used, illustrating the importance of the choice of fitting method. These fits used luminosities measured in the (0.1−2.4) keV band, and temperatures measured with a variable-sized core region removed.

B14 studied a sample of 26 groups with *Chandra* data, which formed an incomplete sample, but for which an estimate of the size of the selection biases was performed. They found a slope of $B_{\rm LT} = 2.17 \pm 0.26$ that increased to 3.20 ± 0.26 when the effects of selection were approximated. These fits used *ROSAT* luminosities corrected to the bolometric band and temperatures measured with *Chandra*, and were performed using BCES *Y*|*X* regression.

Both L14 and B14 found relatively strong steepening of the *L–T* relation when they included a correction for selection effects, while for the 400 d groups sample, our bias correction made a negligible change to the slope compared with the original BCES fit. The fact that we do not see a significant change in the slope when we made the bias correction appears to be due to the fact that our fit without correcting for selection biases was performed with an orthogonal BCES regression, while L14 and B14 primarily used *Y*|*X* regression, which is more sensitive to the selection function since the selection acts in the *Y* direction. If we fit our bolometric with a *Y*|*X* regression, the recovered slope is 2.80 ± 0.22, supporting this interpretation.

Comparisons between bias-corrected *L–T* relation of the 400 d groups sample and the those of L14 and B14 are presented in Fig. 6. For this plot, the L14 and B14 relations were corrected to the (0.5−2) keV band using the method described in Section 4.3. Both the L14 and B14 relations are consistent with the 400 d groups *L–T* relation.

We now take advantage of the growing number of studies of the group *L–T* relation to investigate whether the slope of the *L–T* relation is steeper for groups than for clusters. In Table 7, we summarize the slopes of the bolometric *L–T* relation measured in several studies, along with the median temperature of the sample used to measure the relation. Relations were converted to the bolometric band as described in Section 4.3, and where available we report the bias-corrected slopes. These data are plotted in Fig. 7.

Fig. 7 shows clearly that once selection biases are taken into account, there is no evidence that the *L–T* relation in groups is any steeper than for samples of more massive clusters. This illustrates the importance of correcting selection biases to recover the true underlying population properties.

Table 7. Summary of *L–T* relation slopes from the recent literature. $T_{\rm med}$ is the median temperature of each sample and BC indicates *L–T* relations with bias correction. All the relations are converted into bolometric luminosities as described in the main text. The rows in bold are from this work.

Sample	$T_{\rm med}$	$B_{\rm LT}$
L14	1.4	2.44 ± 0.32
L14 (BC)	1.4	3.25 ± 0.09
B14	1.6	2.17 ± 0.26
B14 (BC)	1.6	3.20 ± 0.26
400 d low-mass	**2.2**	$\mathbf{3.28 \pm 0.33}$
400 d low-mass (BC)	**2.2**	$\mathbf{3.29 \pm 0.33}$
P09	3.9	3.38 ± 0.31
M12	5.8	3.44 ± 0.25
Mantz et al. (2010) (BC)	7.4	3.70 ± 0.55

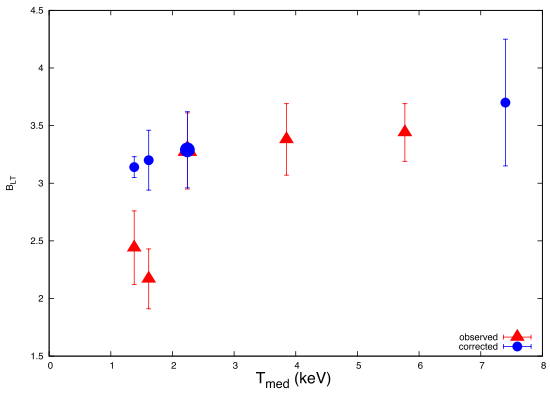

Figure 7. The slope of the *L–T* relation ($B_{\rm LT}$) is plotted against the median temperature ($T_{\rm med}$) of the sample used to measure the relation for samples summarized in Table 7. All of the relations are converted into bolometric *L–T* as described in the text. Red triangles represent fits where selection biases were not included, while blue circles show fits where selection effects were modelled. The points with larger symbols at $T_{\rm med} = 2.2$ keV are from this work.

Based on the results of Schellenberger et al. (2015), in order to compare the slope of an *L–T* relation measured with *Chandra* to one measured with *XMM–Newton*, the slope measured should be multiplied by ≈0.89 to correct for the calibration differences between the instruments. However, the calibration comparisons made by Schellenberger et al. (2015) were almost exclusively limited to temperatures greater than 2 keV. For this reason, it is not clear how well their correction would apply to the low-temperature groups in L14. In principal, the slope measured by P09 could be reduced by an amount roughly the size of the statistical error on their slope to make it consistent with the *Chandra L–T* relations in Fig. 7, but we chose not to apply any correction to the data.

However, there are additional complexities with interpreting this result. It is conventional to compare the slope of the *L–T* relation with the self-similar prediction of $B_{\rm LT} = 2$, but recall that this is the self-similar slope assuming bolometric bremsstrahlung emission; for temperatures below about 2 keV, the contribution of line emission to the total bolometric luminosity becomes significant. This effect is well known, but its implication for interpreting the slope of the *L–T* relation is often overlooked. If the true bolometric bremsstrahlung *L–T* relation of groups and clusters followed the self-similar predictions (i.e. there were no feedback effects), then the observed *L–T* relation would flatten below ∼2 keV due to the increasing addition of line emission to the self-similar bremsstrahlung component. Conversely, if the slope of the bolometric *L–T* relation

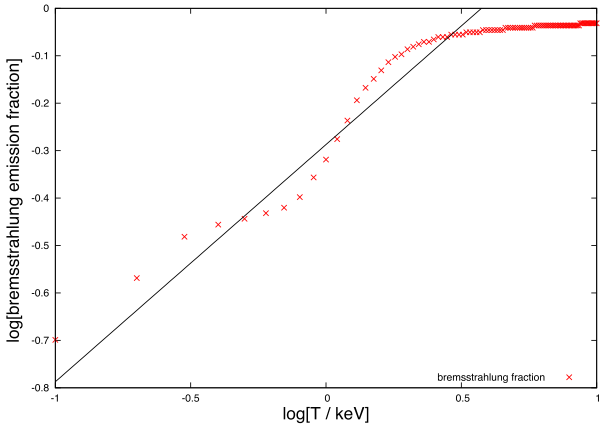

Figure 8. Bremsstrahlung emission fraction ($L_{\rm brem}/L_{\rm tot}$) as a function of temperature. This illustrates the increasing contribution of line emission to the total luminosity for plasmas with $T \lesssim 2$ keV. The solid line is our approximate model of the $T < 2$ keV data.

is observed to be the same for groups and clusters, the implication is that the increasing contribution of line emission is masking a steepening of the underlying bremsstrahlung *L–T* relation.

We estimated the size of this effect on the *L–T* relation with a simplistic approach of measuring the luminosity of APEC spectra with a metal abundance of $Z = 0.3$ ($L_{\rm tot}$), and then setting $Z = 0$ without changing any other parameters to approximate the luminosity of the pure bremsstrahlung component $L_{\rm brem}$. We then used the ratio $L_{\rm brem}/L_{\rm tot}$ to approximate the bremsstrahlung emission fraction for a range of temperatures, and the results are presented in Fig. 8. The increasing contribution of line emission to the total luminosity is clear.

The declining contribution of bremsstrahlung to the total luminosity for $T < 2$ keV was crudely approximated with a power law of the form

$$\frac{L_{\rm brem}}{L_{\rm tot}} = 0.73 \left(\frac{T}{2}\right)^{0.50}, \quad (9)$$

which is plotted in Fig. 8. We thus estimate that for samples with significant numbers of systems below 2 keV, the observed bolometric *L–T* relation could be steeper than the underlying bremsstrahlung *L–T* relation by up to 0.5.

Taking this effect into account, as a first approximation, the $B_{\rm LT}$ values for the 400 d, B14 and M14 samples in Fig. 8 should all be raised by ∼0.5 in order to assess the impact of any feedback. With this extra steepening, the slopes of the group *L–T* relations would remain consistent with the cluster *L–T* relations given the precision of the current measurements, but the effect is large enough that it should be considered in studies of the group *L–T* relation.

It would be useful to directly measure the bolometric bremsstrahlung *L–T* relation from the cluster data to make more direct comparisons with the self-similar model. However, this introduces significant complications in the modelling of selection biases. This is because the clusters are detected on the basis of their total emission (including line emission) so the selection function must be expressed in those terms. Furthermore, clusters are detected in soft-band X-ray imaging, where the contribution of emission lines is even stronger than in the bolometric band. This means that for groups, variations in the metal abundance between systems (perhaps related to their feedback history) could significantly impact the selection function. This makes the problem difficult to unpick observationally, and greater success should result from comparisons of complete X-ray selected group samples with the output of cosmological hydrodynamical simulations, on to which the various observational effects can be applied.

The overall picture that emerges from the comparison of these samples is that the group *L–T* relation is consistent with that of clusters, and that the bolometric bremsstrahlung *L–T* relation has a slope of ≈3–3.5 across the full range of group and cluster samples; always significantly steeper than self-similarity.

5.3 Scatter in the *L–T* relation

In addition to the slope of the *L–T* relation, its intrinsic scatter is a signature of the astrophysical processes affecting the ICM in groups and clusters. Here, we will compare the scatter measured for the 400 d groups sample with measurements from other group and cluster samples. In all cases, the scatter is modelled as lognormal and is reported as the intrinsic scatter in L in natural log space, so corresponds to a fractional scatter. Unless otherwise stated, the scatter values are for core-included luminosities.

In our analysis of the 400 d groups sample, we found a scatter in the bias-corrected soft-band *L–T* relation of $\delta_{\rm LT} = 0.51 \pm 0.15$. For the bolometric *L–T* relation without correction for biases, we found $\delta_{\rm LT} = 0.59 \pm 0.17$, so the scatter was not significantly affected by selection biases. The only other measurement of scatter in the group regime to include an estimate of selection biases was that of B14. They found a scatter of $\delta_{\rm LT} = 0.55$ which increased to $\delta_{\rm LT} = 0.73$ when they approximated the removal of selection biases (errors were not reported, so it is not clear if the change is significant). B14 reported that the bias-corrected scatter in their group sample was larger than that in the cluster sample they used ($\delta_{\rm LT} = 0.62$), however (as B14 noted), this conclusion is limited by the fact that their group sample is incomplete and suffered from archival biases. This could be a significant problem, since the 'interesting' groups in the archives are likely to be among those showing the greatest deviations from the average properties.

The present analysis of the 400 d groups sample is the most robust attempt thus far to measure the scatter in the *L–T* relation including bias corrections. The scatter of 0.51 ± 0.15 we find in the group population is not significantly different from the scatter found for the cluster population in the bias-corrected measurements of B14 (0.62) and Mantz et al. (2010, 0.61 ± 0.15).

5.4 Steepening in the RCC *L–T* relation

In M12, we found that the bolometric *L–T* relation for the subset of the 21 most RCC clusters in our archival *Chandra* sample had a self-similar slope ($B_{\rm LT} = 1.90 \pm 0.14$) with negligible scatter, when the central $0.15R_{500}$ was excluded. We found a suggestion that the slope of this core-excluded RCC relation might steepen below about 3.5 keV but lacked sufficient numbers of low-mass systems to make a clear measurement. With the addition of the 400 d groups sample, we can extend this test to these lower mass objects.

In Fig. 9, we plot the five RCC clusters from our sample along with the RCC clusters from M12 and the CC clusters from P09. The 400 d points are clearly inconsistent with an extrapolation of the self-similar M12 relation, but along with the lower temperature P09 clusters, the data strongly suggest a steepening of the *L–T* relation below about 3 keV. Recall that the 400 d groups sample has been analysed in a manner consistent with M12, and the core-included *L–T* relations agree well (Fig. 2). Some evidence for steepening in the *L–T* relation is seen in the core-excised plot in Fig. 2, but this is more apparent in the RCC subsample shown in Fig. 9, primarily

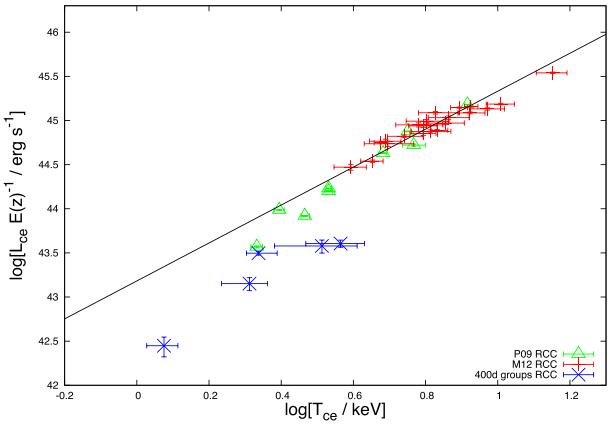

Figure 9. The bolometric *L–T* relation for RCC clusters from M12 and the 400 d groups sample, and CC clusters from P09. Luminosities and temperatures were measured in the (0.15–1)R_{500} aperture. The solid line is the best fit to the M12 data.

because of the much flatter self-similar slope of the M12 RCC clusters.

Putting these results together with the previous section, we find that when the core regions of clusters are included, the *L–T* relation of groups is consistent in every way with that of clusters. However, when core regions are removed, and particularly for the most RCC clusters, the slope of the *L–T* relation steepens from a self-similar value in the cluster population (M12) to a steeper value below ∼3 keV.

6 SUMMARY

This work presented the *L–T* relation of 23 low-mass galaxy clusters and groups selected from the 400 d survey. The systems were all observed with *Chandra*, and the analysis of the *L–T* relation included a Bayesian modelling of the selection biases. The following were the main results of this work.

(i) The effect of selection biases on the 400 d groups sample is not large; our correction for the selection biases did not significantly change any of the *L–T* relation parameters.

(ii) The core-included *L–T* relation of the 400 d groups sample was consistent with the *L–T* relations found in clusters, and significantly steeper than self-similar predictions. Indeed, when combined with other recent studies of the *L–T* relation in groups, and once selection biases are corrected, there is no evidence that the slope of the (core included) group *L–T* relation is different from that of massive clusters.

(iii) The intrinsic scatter of the *L–T* relation (with cores included) of the 400 d groups is ≈50 per cent and is consistent with the scatter in the *L–T* relation found in cluster samples.

(iv) While the magnitude of the scatter in the 400 d groups *L–T* relation is consistent with that found for more massive clusters, it is not driven by the luminosity of the core regions in the same way as for cluster samples. Instead, the scatter in the 400 d groups relation seems to be driven by the dynamical state of the clusters.

(v) The increasing contribution of line emission to the luminosity of lower temperature systems means that the bolometric *L–T* slope measured in the group regime is flatter by ≈0.5 than the underlying bolometric bremsstrahlung *L–T* relation slope. The latter is what is predicted by the self-similar model, so this effect could (partially) mask processes that are removing gas from lower mass systems. In this study, taking this effect into account would not change the conclusion that the slope of the *L–T* relation is consistent for groups and clusters.

(vi) For the particular case of RCC systems, we find that the 400 d groups lie significantly below the self-similar core-excised *L–T* relation found for massive RCC clusters. This suggests a significant steepening of the core-excised RCC *L–T* relation below about 3 keV.

Overall, our work is the most rigorous attempt so far to measure the *L–T* relation in the group regime, including the correction for selection biases. These results thus provide a secure basis against which to test feedback models in hydrodynamical simulations. Those models are often tested against data for which selection biases have not been modelled (e.g. Short et al. 2010; Le Brun et al. 2014). Studies like ours provide corrected scaling relations that can be compared directly with the simulations. For future work, an improved analysis would relax the assumption of a fixed *M–T* relation with no scatter and instead use a multivariate analysis to model the luminosity, temperature and $M_{\rm gas}$ of low-mass clusters simultaneously (as in e.g. Mantz et al. 2010; Evrard et al. 2014; Maughan 2014; Ettori 2015). However, this would require an observable that was a direct proxy for cluster mass, such as weak lensing mass, which is currently very challenging to obtain at these masses.

ACKNOWLEDGEMENTS

BJM and PAG acknowledge support from STFC grants ST/J001414/1 and ST/M000907/1.

RB was supported by RNF grant 14-22-00271.

REFERENCES

Akritas M. G., Bershady M. A., 1996, ApJ, 470, 706
Arnaud K. A., 1996, in Jacoby G. H., Barnes J., eds, ASP Conf. Ser. Vol. 101, Astronomical Data Analysis Software and Systems V. Astron. Soc. Pac., San Francisco, p. 17
Bharadwaj V., Reiprich T. H., Lovisari L., Eckmiller H. J., 2015, A&A, 573, A75 (B14)
Burenin R. A., Vikhlinin A., Hornstrup A., Ebeling H., Quintana H., Meshcheryakov A., 2007, ApJS, 172, 561
Churazov E., Sunyaev R., Forman W., Böhringer H., 2002, MNRAS, 332, 729
Eckmiller H. J., Hudson D. S., Reiprich T. H., 2011, A&A, 535, A105
Edge A. C., Stewart G. C., 1991, MNRAS, 252, 414
Ettori S., 2015, MNRAS, 446, 2629
Evrard A. E., Arnault P., Huterer D., Farahi A., 2014, MNRAS, 441, 3562
Fabian A. C., 1994, ARA&A, 32, 277
Fabian A. C., 2012, ARA&A, 50, 455
Finoguenov A., Reiprich T. H., Böhringer H., 2001, A&A, 368, 749
Fruscione A. et al., 2006, in Silva D. R., Doxsey R. E., eds, Proc. SPIE Conf. Ser. Vol. 6270, Observatory Operations: Strategies, Processes, and Systems. SPIE, Bellingham, p. 62701
Helsdon S. F., Ponman T. J., 2000, MNRAS, 315, 356
Hlavacek-Larrondo J. et al., 2015, ApJ, 805, 35
Hofmann F., Sanders J. S., Nandra K., Clerc N., Gaspari M., 2016, A&A, 585, A130
Kaiser N., 1986, MNRAS, 222, 323
Kettula K. et al., 2015, MNRAS, 451, 1460
Khosroshahi H. G., Ponman T. J., Jones L. R., 2007, MNRAS, 377, 595
Le Brun A. M. C., McCarthy I. G., Schaye J., Ponman T. J., 2014, MNRAS, 441, 1270
Lovisari L., Reiprich T., Schellenberger G., 2015, A&A, 573, A118 (L14)
Ma C.-J., McNamara B. R., Nulsen P. E. J., Schaffer R., Vikhlinin A., 2011, ApJ, 740, 51
McNamara B. R., Nulsen P. E. J., 2007, ARA&A, 45, 117

Mantz A., Allen S. W., Ebeling H., Rapetti D., Drlica-Wagner A., 2010, MNRAS, 406, 1773
Markevitch M., 1998, ApJ, 504, 27
Maughan B. J., 2007, ApJ, 668, 772
Maughan B. J., 2014, MNRAS, 437, 1171
Maughan B. J., Giles P. A., Randall S. W., Jones C., Forman W. R., 2012, MNRAS, 421, 1583 (M12)
Mulchaey J. S., Zabludoff A. I., 1998, ApJ, 496, 73
Osmond J. P. F., Ponman T. J., 2004, MNRAS, 350, 1511
Pacaud F. et al., 2007, MNRAS, 382, 1289
Pacaud F. et al., 2016, A&A, 592, A2
Panagoulia E. K., Fabian A. C., Sanders J. S., Hlavacek-Larrondo J., 2014, MNRAS, 444, 1236
Peterson J. R., Fabian A. C., 2006, Phys. Rep., 427, 1
Pratt G. W., Croston J. H., Arnaud M., Böhringer H., 2009, A&A, 498, 361 (P09)
R Core Team 2014, R: A Language and Environment for Statistical Computing. R Foundation for Statistical Computing. Vienna, Austria, available at: http://www.R-project.org
Randall S. W. et al., 2015, ApJ, 805, 112
Rowley D. R., Thomas P. A., Kay S. T., 2004, MNRAS, 352, 508
Sahlén M. et al., 2009, MNRAS, 397, 577
Schellenberger G., Reiprich T. H., Lovisari L., Nevalainen J., David L., 2015, A&A, 575, A30
Short C. J., Thomas P. A., Young O. E., Pearce F. R., Jenkins A., Muanwong O., 2010, MNRAS, 408, 2213
Smith R. K., Brickhouse N. S., Liedahl D. A., Raymond J. C., 2001, ApJ, 556, L91
Statisticat LLC, 2016, LaplacesDemon: Complete Environment for Bayesian Inference. R package version 16.0.1. Available at: http://www.bayesian-inference.com/software
Sun M., 2009, ApJ, 704, 1586
Sun M., Voit G. M., Donahue M., Jones C., Forman W., Vikhlinin A., 2009, ApJ, 693, 1142
Tinker J., Kravtsov A. V., Klypin A., Abazajian K., Warren M., Yepes G., Gottlöber S., Holz D. E., 2008, ApJ, 688, 709
Vikhlinin A., McNamara B. R., Forman W., Jones C., Quintana H., Hornstrup A., 1998, ApJ, 502, 558
Vikhlinin A., Markevitch M., Murray S. S., Jones C., Forman W., Van Speybroeck L., 2005, ApJ, 628, 655
Vikhlinin A., Burenin R., Forman W. R., Jones C., Hornstrup A., Murray S. S., Quintana H., 2007, in Böhringer H., Pratt G. W., Finoguenov A., Schuecker P., eds, Heating versus Cooling in Galaxies and Clusters of Galaxies. Springer-Verlag, Berlin, p. 48
Vikhlinin A. et al., 2009a, ApJ, 692, 1033
Vikhlinin A. et al., 2009b, ApJ, 692, 1060

APPENDIX A: ANALYSIS OF RXJ1416.4+2315

RXJ1416.4+2315 (obsid = 2024) is an unusual case, with an unrealistically high temperature (up to ∼20 keV) in our initial analysis. Upon inspection of the light curve and background spectrum, the observation was found to be affected by low-level background flaring throughout the observation. For this reason, a bespoke analysis was performed.

We produced a residual background spectrum of RXJ1416.4+2315, as for our analyses of the other targets, but in this case it was modelled with the standard thermal component plus an additional power-law component. Here, the power law models the extra particle-induced background in this observation, and so was not folded through the instrument effective area. Fig. A1 shows the residual spectrum modelled by a thermal model alone (our standard analysis); the residuals are systematically high above ∼1keV. Fig. A2 shows the same residual background spectrum modelled with an additional power-law component. This background model was then included as an extra additive model when fitting the cluster spectrum. We included an extra systematic component to the errors on the temperature and normalization of the cluster APEC model by fixing the slope and normalization of the extra power-law component at their $\pm 1\sigma$ errors and refitting the cluster thermal component. The maximum change in the cluster temperature and normalization were used as an estimate of their systematic uncertainty due to the extra background component. These systematic errors were very similar in size to the original statistical errors, and were added in quadrature to the statistical uncertainties on the derived cluster properties.

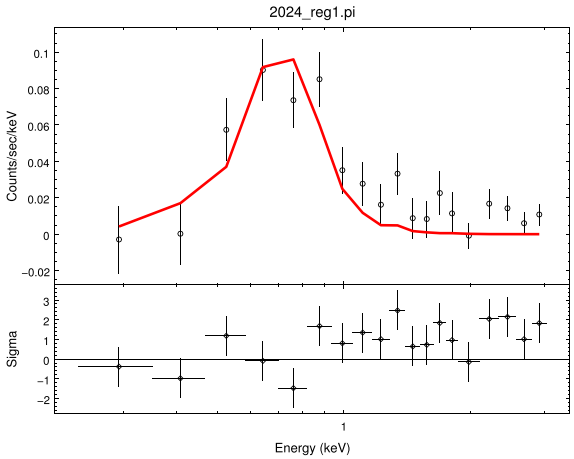

Figure A1. The background residual spectrum for cluster RXJ1416.4+2315 is shown with the best-fitting APEC thermal model. Residuals in units of σ are shown in the bottom panel.

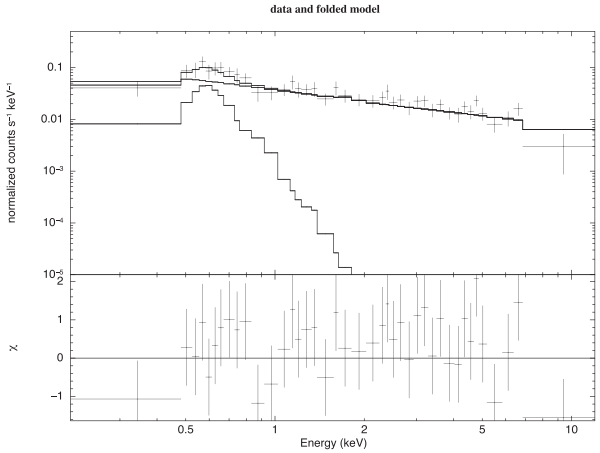

Figure A2. The background residual spectrum for cluster RXJ1416.4+2315 is shown with the best-fitting APEC plus power-law model. Residuals in χ^2 are shown in the bottom panel.

This paper has been typeset from a TEX/LATEX file prepared by the author.